APPLIED SCIENCES AND ENGINEERING

A swarm of slippery micropropellers penetrates the vitreous body of the eye

Zhiguang Wu[1,2], Jonas Troll[3], Hyeon-Ho Jeong[1], Qiang Wei[4], Marius Stang[5], Focke Ziemssen[5], Zegao Wang[6], Mingdong Dong[6], Sven Schnichels[5], Tian Qiu[1]*, Peer Fischer[1,3]*

The intravitreal delivery of therapeutic agents promises major benefits in the field of ocular medicine. Traditional delivery methods rely on the random, passive diffusion of molecules, which do not allow for the rapid delivery of a concentrated cargo to a defined region at the posterior pole of the eye. The use of particles promises targeted delivery but faces the challenge that most tissues including the vitreous have a tight macromolecular matrix that acts as a barrier and prevents its penetration. Here, we demonstrate novel intravitreal delivery microvehicles—slippery micropropellers—that can be actively propelled through the vitreous humor to reach the retina. The propulsion is achieved by helical magnetic micropropellers that have a liquid layer coating to minimize adhesion to the surrounding biopolymeric network. The submicrometer diameter of the propellers enables the penetration of the biopolymeric network and the propulsion through the porcine vitreous body of the eye over centimeter distances. Clinical optical coherence tomography is used to monitor the movement of the propellers and confirm their arrival on the retina near the optic disc. Overcoming the adhesion forces and actively navigating a swarm of micropropellers in the dense vitreous humor promise practical applications in ophthalmology.

INTRODUCTION

Ocular drug delivery plays an important role in ophthalmology and is used to treat diseases ranging from diabetic retinopathy, glaucoma, to diabetic macular edema (*1*). Although topical administration is currently available to treat diseases in the anterior of the eye including the cornea, ciliary body, and the lens (*2*), delivery to the posterior part of the eye via topical administration, systemic administration, and intravitreal injection is very ineffective and difficult because of the lacrimal fluid–eye barrier and the retina–blood barrier (*3*, *4*). To overcome these difficulties, nanoparticles have been injected into the eye, and their passive diffusion toward the retina has been investigated (*5*–*7*). Passive diffusion, however, suffers from long diffusion time and decreased activity of the biomedical agents (*8*). Moreover, it is systemic and therefore comes with an increased risk of side effects (*9*). It therefore still remains challenging to achieve targeted delivery with intravitreal administration.

In contrast, actively propelled micro- and nanoparticles provide a novel potential pathway for the targeted delivery of drugs in the human body (*10*–*13*). A few synthetic microparticle systems that can be actively propelled in biological media have been developed. These have predominantly focused on propulsion in liquids or fluid-filled cavities in the body, such as chemically propelled structures that can move in the low-pH fluids of the stomach (*14*–*16*) or magnetically propelled structures that can move in blood (*17*–*19*). A swarm of magnetic propellers has also been moved and imaged in the stomach of a mouse (*20*). In addition, it has been shown that an enzymatic coating of microparticles can facilitate the penetration of mucus (*21*). The translation of a larger cylindrical magnetic structure (~285 μm in outer diameter and ~1800 μm in length) that is moved by a magnetic gradient field is reported to be restricted in the vitreous (*22*). The propulsion in the vitreous over long distances has not yet been realized because of the strong obstruction by the biopolymer network. We demonstrate that sufficiently small structures that are wirelessly actuated are able to efficiently move through vitreous, when they are equipped with a suitable surface chemistry.

Active microrheology shows that the mesh size of the (porcine) vitreous is ~500 nm, suggesting that nanoparticles with sizes well below this threshold can move relatively unhindered, provided that they do not experience any adhesion (*23*). Moreover, we reported that magnetic helical nanopropellers of ~120 nm in diameter and ~400 nm in length are able to propel in nanoporous hyaluronan solutions, a model fluid mimicking the vitreous (*24*). These results indicate that if the size of the propellers is much smaller than the mesh size of the complex network, then their interaction with the polymeric network is minimized; therefore, the propulsion of nanopropellers, but not larger micropropellers, is possible in the nanoporous medium. However, both the propulsive speed and load capacity of nanopropellers are limited because of their small size. Therefore, it is beneficial to nevertheless increase the propeller size as much as possible, while facilitating the penetration of the porous biological media.

Here, we report the first micropropellers that can penetrate the vitreous humor and that can reach the retina. The propellers are helical in shape, with the diameter that is comparable to the mesh size of the biopolymeric network of the vitreous and are functionalized with a perfluorocarbon surface coating that minimizes the interaction of the propellers with biopolymers, including collagen bundles that are present in the vitreous. The coating is inspired by a liquid layer found on the carnivorous *Nepenthes* pitcher plant, which presents a slippery surface on the peristome to catch insects (*25*–*27*). The nontoxic silicone oil and fluorocarbon coatings are also used as slippery surfaces in medical applications (*28*, *29*). Under the wireless actuation of an external magnetic field, the coated micropropellers not only show

[1]Max Planck Institute for Intelligent Systems, Heisenbergstrasse 3, 70569 Stuttgart, Germany. [2]Key Laboratory of Microsystems and Microstructures Manufacturing, Ministry of Education, Harbin Institute of Technology, Yi Kuang Jie 2, Harbin 150080, China. [3]Institute of Physical Chemistry, University of Stuttgart, Pfaffenwaldring 55, 70569 Stuttgart, Germany. [4]Max Planck Institute for Medical Research, Jahnstraße 29, 69120 Heidelberg, Germany. [5]Center of Ophthalmology, University Eye Hospital Tübingen, Tübingen, Germany. [6]Interdisciplinary Nanoscience Center (iNANO), Aarhus University, Aarhus C, Denmark.
*Corresponding author. Email: qiu@is.mpg.de (T.Q.); fischer@is.mpg.de (P.F.)

controllable propulsion but also can be driven as a large swarm over centimeter distances through the eyeball and can reach the retina within 30 min. The micropropellers are imaged with standard optical coherence tomography (OCT).

We expect that the complete operating procedure (as demonstrated in Fig. 1), including intravitreal injection, long-range self-propulsion, and noninvasive monitoring via a clinically approved instrument, advances the targeted delivery with a view toward future ophthalmological therapies.

RESULTS

Fabrication and perfluorocarbon surface coating of the slippery micropropellers

The fabrication of the slippery micropropellers consists of two main steps: the preparation of helical microstructures and their coating (Fig. 2A). The helical microstructures were fabricated using physical vapor shadow growth via glancing angle deposition (GLAD) (*30*, *31*), as previously described (*21*, *32*). The helices were deposited with a body of silica as the structural element and nickel (or iron) as the magnetic segment (see Materials and methods for details). The surface functionalization consisted of a gas phase deposition of a perfluorosilane and the subsequent fusion with a slippery perfluorocarbon liquid layer (*33*). Last, the slippery microhelices were released from the wafer with ultrasound and well dispersed into aqueous media. The fusion of the perfluorocarbon liquid onto the perfluorocarbon molecule–functionalized microhelices results in a fully covered and durable liquid surface layer.

The scanning electron microscope (SEM) image in Fig. 2B shows many structurally identical microhelices on part of a silicon wafer. Billions of microhelices are obtained on a 51-mm diameter wafer in a single fabrication process. The enlarged ESB (energy-selective backscatter)–SEM image Fig. 2B shows the presence of the nickel segment and the typical helix geometry with a length of 2 μm and a silica head of 500 nm in diameter, which approximately matches the mesh size of network in the vitreous. Figure 2C shows that the contact angles of the array of uncoated microhelices and of the perfluorocarbon liquid layer–functionalized microhelices are 8° ± 1° and 146° ± 1°, respectively. The large increase of the water contact angle verifies the effective enhancement of the hydrophobicity and the decrease of the surface energy by the coating. Furthermore, Fourier transform infrared (FTIR) spectroscopy (Fig. 2C) shows that the coated micropropellers show infrared peaks assigned to the perfluorocarbon liquid, which confirms the successful functionalization with the perfluorocarbon materials.

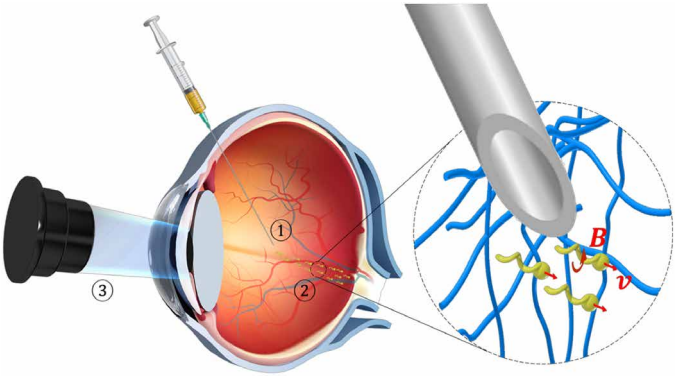

Fig. 1. Schematic of the three-step targeted delivery procedure used for the slippery micropropellers. (1) Injection of the micropropellers into the vitreous humor of the eye. (2) Magnetically driven long-range propulsion of the micropropellers in the vitreous toward the retina. (3) Observation of the micropropellers at the target region near the surface of the retina by OCT.

Controlled propulsion in the vitreous

Porcine eyes are often used as model systems for human eyes because of similarities in the anatomy and similar properties of the vitreous (*34*). The micropropellers were driven wirelessly via a rotating magnetic field with an amplitude of 8 mT (80 G). To confirm that the propulsion occurred inside the vitreous, we injected a mixture of micropropellers and passive silica microparticles into the vitreous and was subjected it to a rotating magnetic field. As expected, only the micropropellers did penetrate the vitreous (fig. S1). The time-lapse images in Fig. 3A show the rotation of an uncoated micropropeller for one period with a magnetic field of 8 mT at a relatively low rotation frequency of 6 Hz (to facilitate observation). The uncoated propeller is unable to complete one full rotation and only exhibits a wobbling motion, i.e., not rotating around the helix's long axis (movie S1). In contrast, the corresponding time-lapse images in Fig. 3B (movie S2) show that a single slippery propeller, with the same magnetic actuation parameters as the uncoated propellers, can rotate around its long axis, and it propels forward within 1.5 s (nine periods). The rotation angle $\alpha = d/p \times 360^{\circ}$, where p is the pitch of the helix, was quantified by measuring the distance d between the crest and the head of the propeller (Fig. 3, A and B). As shown in Fig. 3C, the rotation angle of the slippery propeller continuously changes from 0° to 360°, which corresponds to a complete rotation over one period. However, the uncoated helix propeller shows hindered motion and only reorients slightly before returning to its starting position (0°). We ascribe this behavior to adhesion to the vitreous. The data reveal that the slippery liquid coating layer is crucial for the propulsion of the micropropellers in the vitreous, and this is also reflected in the Brownian diffusion coefficients of coated and uncoated particles (Fig. 3D). In agreement with previous measurements (*6*), the diffusion coefficient decreases as the particle size increases. In particular, 1-μm particles display only minor or negligible diffusion in the vitreous. The slippery particles, however, show much higher diffusion coefficients compared with uncoated silica particles in the vitreous, with ~7- and ~5-fold enhancements, respectively, for the 300- and 500-nm particles (Fig. 3D).

We find that only a small fraction of the micropropellers can propel in the vitreous if they are only functionalized with the perfluorocarbon molecules (fig. S2A). However, with the fluorocarbon liquid layer, the micropropellers show efficient propulsion and sustain their propulsion over long (centimeter) distances. The coating thus is crucial, and its liquid nature affords a defect-free coverage, considerable pressure stability, and a self-healing effect (*26*). The time-lapse image in fig. S2B and movie S3 show that a large population of the slippery micropropellers moves from the aqueous buffer across the boundary into the vitreous (fig. S2C). It should be noted that, besides nickel, it is also possible to grow micropropellers with more biocompatible materials, such as iron (fig. S3). We show that slippery propellers made of Fe and TiO_2 material also display controlled intravitreal propulsion when actuated by the external rotating magnetic field (fig. S4). Statistical analysis shows that the intravitreal propulsion is not affected by the use of these other materials (fig. S5). Moreover, we find that the perfluorocarbon liquid layer is

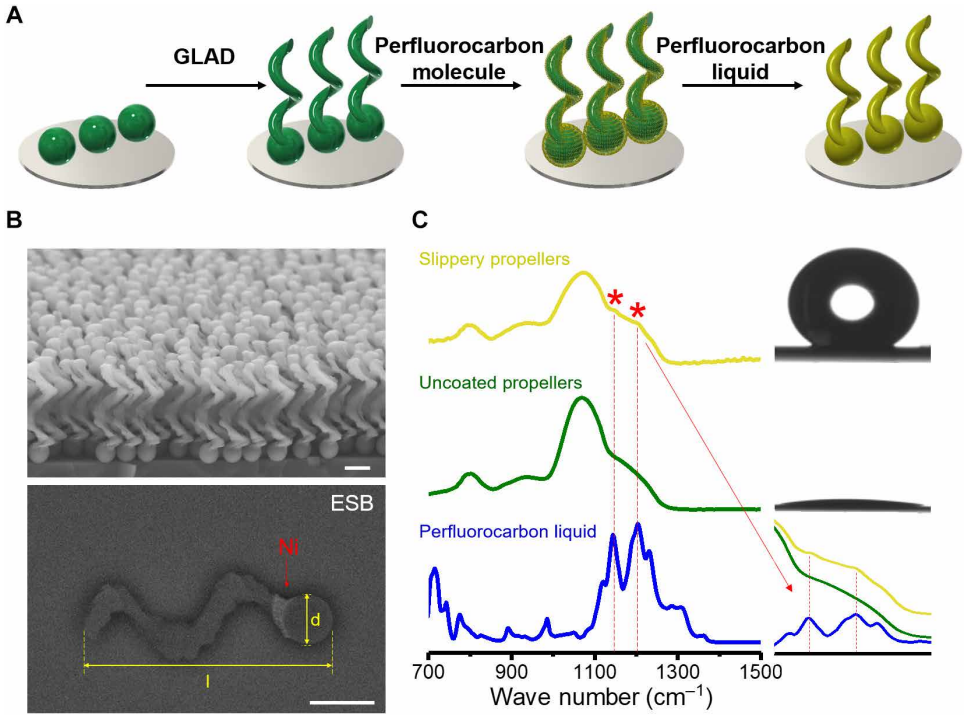

Fig. 2. Fabrication and characterization of the perfluorocarbon-coated "slippery" micropropellers. (**A**) Schematic of the fabrication process. (**B**) SEM (top) and ESB-SEM (bottom) images of the micropropellers. The yellow arrows indicate the length (l) of the propeller and the diameter (d) of the head of the propeller. The white area is the nickel part of the propeller. Scale bars, 500 nm. (**C**) FTIR spectroscopy of the micropropellers without coating and with the perfluorocarbon coating, and the perfluorocarbon liquid. The enlarged spectra are displayed at the bottom right, proving the presence of the perfluorocarbon. The contact angles of the wafer with an array of coated helices (top) and uncoated helices (bottom) are shown, respectively.

stable over time and that the coated micropropellers are still able to move in the vitreous after more than a month of storage under ambient conditions.

The micropropellers rotate and thus translate for magnetic field strengths above 2.5 mT (fig. S8). A high percentage of micropropellers move when exposed to a physiological buffer and solution for 2 hours (fig. S6 and table S1). Using quantitative dynamic atomic force microscopy (AFM), we demonstrate in fig. S7 that the liquid perfluorocarbon coating lowers the adhesion force significantly (the bare surface: 10.0 ± 5.0 nN, the coated surface: 4.0 ± 2.4 nN). The adhesion force of the slippery propellers exhibits only minor changes after exposure to physiological buffer and shaking for 2 hours (4.6 ± 1.5 nN), indicating good stability of the slippery coating on the micropropellers. The movement direction of the micropropellers is controlled in real time through the manipulation of the external magnetic field. The time-lapse image in Fig. 3E shows that the propellers follow controlled paths in the vitreous (movie S4). The velocity depends on the rotational frequency of the magnetic field. As shown in Fig. 3F, the average velocity in water increases from 1.4 μm/s at 10 Hz to 11.4 μm/s at 100 Hz. The propulsion in the vitreous exhibits a similar trend over the 10- to 70-Hz range from 0.7 to 10.6 μm/s. The step-out frequency (when the propeller can no longer rotate in synchrony with the external magnetic field) in the vitreous is 70 Hz, which is lower than that in water (100 Hz), indicating that the dynamic viscosity is higher and approximately 1.4 centipoise (cP), which is similar to the dynamic viscosity of porcine vitreous (1.6 cP) according to the literature (*34*).

Propulsion behavior in heterogeneous media

The heterogeneity of the vitreous results in unique locomotion behavior compared with that in other model fluids. Two typical trajectories observed in the vitreous are shown in Fig. 4A. We observed that some propellers can be stuck before resuming their movement in the vitreous, which is typically not observed in homogeneous viscoelastic media (*24*). As shown in the histogram in Fig. 4B, the dynamic velocity in an aqueous glycerol solution (~25%) displays a narrower speed distribution, ranging from 5 to 20 μm/s. In contrast, the dynamic velocity in the vitreous ranges from 0 to 40 μm/s. More than 5% of propellers temporally show no propulsion, suggesting that they are occasionally stuck.

Furthermore, the micropropellers translating in the vitreous show larger deviations in their pointing angle compared to those moving in homogeneous glycerol solutions, as the trajectories in fig. S9A show. To quantify the locomotion in heterogeneous media, we examine the dynamic swing angle (SA)—defined as the angle between the instantaneous pointing direction and the target direction (the rotational axis of the external magnetic field), as illustrated in fig. S9A. We statistically analyzed more than 1000 instantaneous velocities of the propellers in the vitreous and glycerol solution, respectively. The results in fig. S9 suggest that, in the glycerol solution, the majority (~75%) of the SA lies in the range of −10° to 10°, and ~96% of SA is in the range of −45° to 45°. In comparison, the distribution of SA in the vitreous is wider, ~48% lies within −10° to 10°, and ~84% the SA varies from −45° to 45°, but the average intravitreal propulsion direction is still maintained. The large SA in the

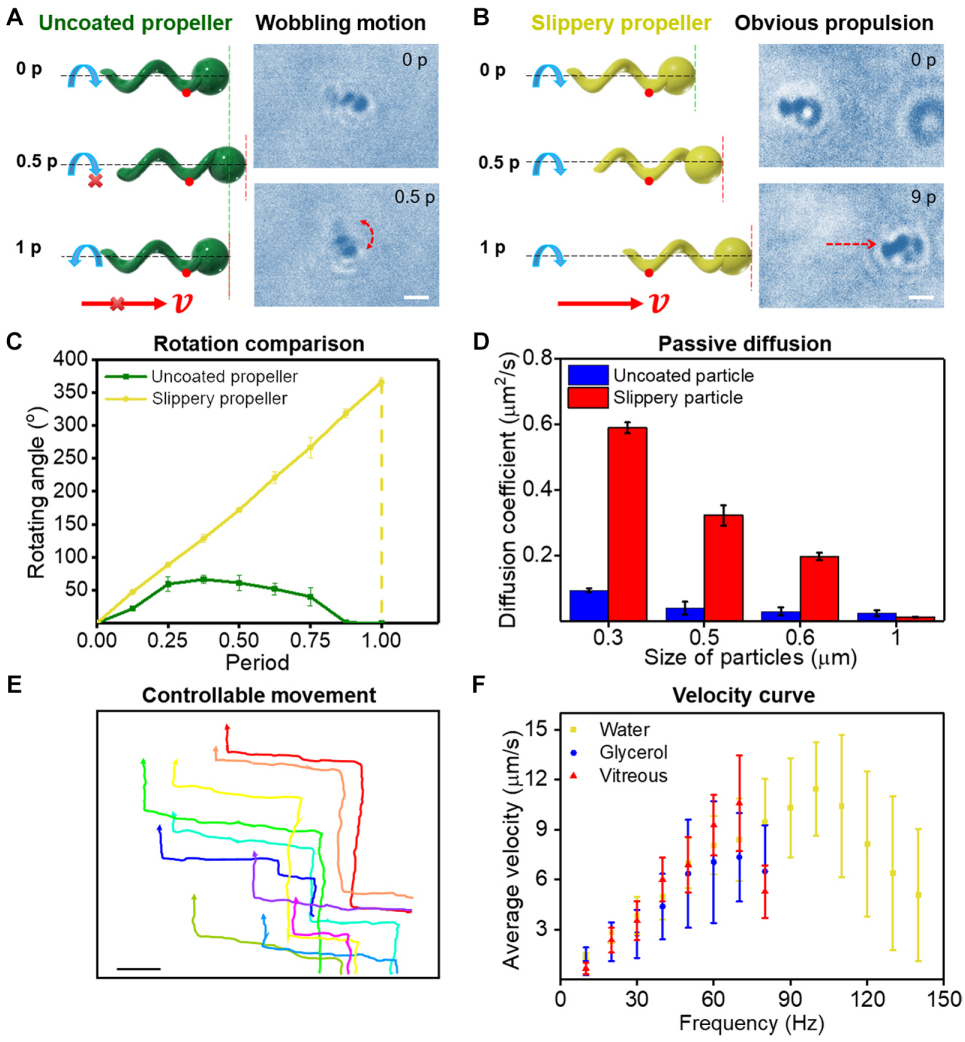

Fig. 3. Controllable movement of the perfluorocarbon-coated micropropellers in the vitreous humor. (**A**) Schematic and time-lapse microscopy images showing the incomplete rotation of an uncoated micropropeller for one period (p) in the vitreous. (**B**) Schematic and time-lapse images showing the magnetically powered propulsion of the coated slippery propeller in the vitreous for 1.5 s (nine periods). In both schematic images, the green and the red dashed lines indicate the original position of the particles and the position of the particles during the application of the rotating magnetic field, respectively. The red arrows in both figures indicate the propulsion direction of the propeller. Scale bars, 1 μm. (**C**) Rotation angle of the uncoated propeller and the slippery propeller in the vitreous under the application of a rotating magnetic field. (**D**) Measured passive diffusion coefficients of uncoated silica particles and the slippery layer–functionalized particles in the vitreous. (**E**) Controllable magnetic field–driven propulsion of the coated micropropellers in the vitreous. The lines indicate the trajectories of the propellers (movie S4). Scale bar, 20 μm. (**F**) Dependence of the propulsion velocity of the slippery micropropellers on the driving frequency of the magnetic field in the vitreous, 25% glycerol solution, and water, respectively. Error bars represent SDs.

vitreous indicates that the propellers frequently change their direction while navigating the heterogeneous collagen network of the vitreous.

Although the SA diverges in the vitreous, the slippery micropropellers demonstrate negligible deviation over their long-range propulsion, given by the external rotating magnetic field. The trajectories in Fig. 4C show the horizontal propulsion (in the intended X direction) of the three slippery micropropellers in vitreous, with a total travel distance of 100 μm, while their vertical displacements (in Y direction) are below 5 μm. As shown in Fig. 4D, the target angle (TA) is defined as $TA = \tan^{-1}(d_v/d_h)$, where d_v and d_h are the vertical and horizontal displacements, respectively. TA is the measure of the ability of the micropropellers to reach a target over longer distances, and the corresponding statistics is shown in Fig. 4D. The data confirm the precise directionality during the magnetic propulsion of the slippery micropropellers in the vitreous despite large short-time fluctuations.

Long-range propulsion of coated micropropellers observed with an OCT system

To investigate the propulsion of micropropellers in an intact eye, we loaded the propellers with fluorescent nanodiamonds for fluorescence imaging. As shown in Fig. 5A, a mixture (~100 μl) containing the fluorescence-labeled micropropellers and passive fluorescent microparticles (20 μm in diameter) was injected close to the center of an intact (resected) porcine eye. The deposition of a thin Al_2O_3

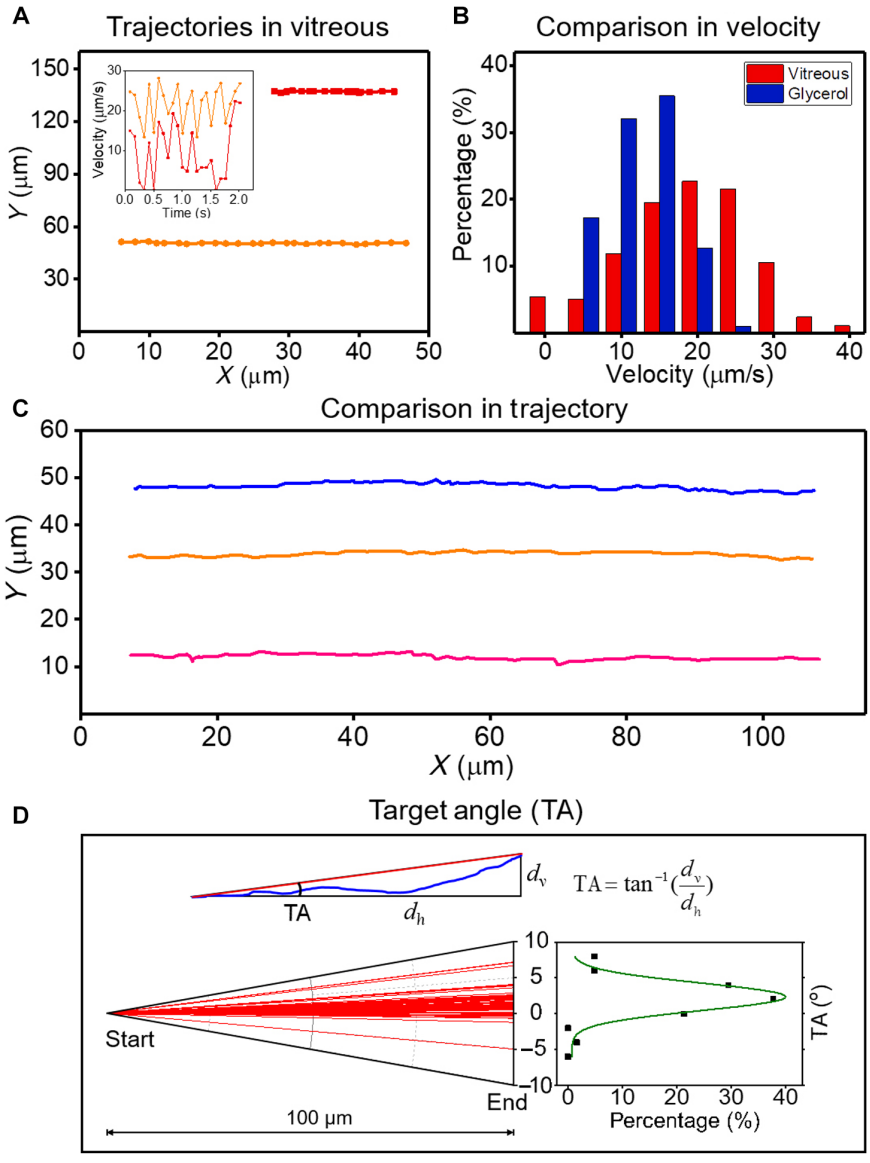

Fig. 4. Characterization of the movement the slippery micropropellers in the vitreous. (**A**) Two typical trajectories of the micropropellers and their corresponding dynamic velocities (inset). (**B**) Histograms of the dynamic velocities of the microhelices in the vitreous and 25% glycerol. (**C**) Flexural trajectories of the slippery micropropellers in the vitreous over a horizontal distance of 100 μm. (**D**) Directionalities between the start and end points over a horizontal distance of 100 μm. The distribution of the TA of the micropropellers in the vitreous is statistically analyzed ($n > 60$).

layer before the fluorescence functionalization provides a chemically uniform coating of the micropropellers and facilitates the coating with the slippery surface. The statistical analysis of the intravitreal propulsion in fig. S5 demonstrates that the thin Al_2O_3 coating and the use of Fe instead of Ni do not adversely affect the movement of the slippery propellers in the vitreous (fig. S5 and table S1). Subsequently, we placed the porcine eye in the rotating magnetic field for 30 min, so that the propellers could move to the retina. The eye was then carefully opened, and the vitreous was mechanically removed. The retina was cut into six pieces (~1 cm by 1 cm each). The retina cell nuclei were stained with 4′, 6-diamidino-2-phenylindole (DAPI) (see Materials and methods for details) and imaged by fluorescence microscopy. We observed red fluorescence on the retina segment that contained the expected target region (Fig. 5B). In contrast, two negative control groups were conducted. In the first control group, propellers and passive particles were injected into the eye, but no magnetic field was applied. After 30 min, no obvious red fluorescence was observed on the retina (fig. S10B), indicating, as expected, that the propellers cannot diffuse through the vitreous and reach the retina without magnetic propulsion. In the second control group, an area of the retina that is away from the target region (optic disc) was observed after the magnetic propulsion (fig. S10C), and no red fluorescence was found, which supports the precise target-reaching ability of the micropropellers.

One major challenge is to image artificial micro- and nanopropellers with a suitable technique in vivo (*35*).We therefore used a standard clinical OCT instrument for the observation of the micropropellers close to the retina in a noninvasive and label-free manner. After

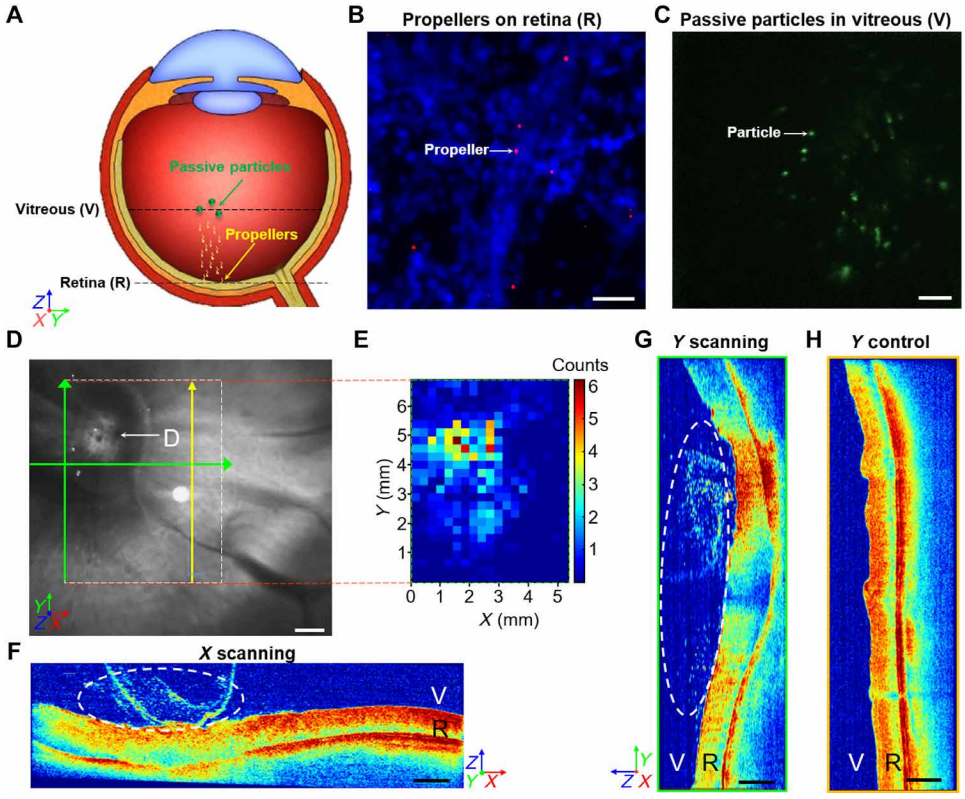

Fig. 5. Movement of the slippery micropropellers in the complete eyeball. (**A**) Schematic illustrating the movement of the slippery micropropellers in the vitreous (V) toward the retina (R). Passive fluorescent particles are injected with the micropropellers to mark the injection position. (**B**) Fluorescent microscopy image of the incised retina at the target region after the magnetic propulsion. Micropropellers [loaded with fluorescent nanodiamonds (red)] are observed on the retina [cell nuclei stained by DAPI (blue)]. Scale bar, 20 μm. (**C**) Fluorescence image shows that the passive fluorescent particles are located near the center of the vitreous. Scale bar, 1 mm. (**D**) Autofluorescence image of the retina near the optic disc. "D" stands for optic disc. Scale bar, 1 mm. (**E**) Colormap calculated by the three-dimensional (3D) reconstruction of the OCT scans, showing the distribution of the micropropellers in the corresponding dashed-line box in (D). (**F** and **G**) OCT images of *X* and *Y* scans, respectively, near the propellers' landing zone. The dashed-line circles label the region of the micropropellers near the retina. The scan planes are indicated as green arrows in (D). (**H**) OCT image of the Y scan away from the optic disc, indicated as the yellow arrow in (D). Scale bars, 500 μm in (F to H).

magnetic actuation, we placed the intact eye in front of a clinical imaging platform that combines scanning laser ophthalmoscopy (SLO) and OCT (see Materials and methods for details). The passive fluorescent microparticles were used as a label to locate and mark the intravitreal injection spot. The fluorescence image acquired with the scanning laser imaging modality is shown in Fig. 5C, which indicates that the passive fluorescent particles remain near the center of the vitreous of the eye. In contrast, the OCT scans of the vitreous-retina boundary reveal the swarm of micropropellers both on the retina and very close to it (Fig. 5, D to H, and movie S5). Figure 5D shows the autofluorescence image of the retina, in which the optic disc (labeled as D) is seen in the top left. The corresponding cross-sectional OCT images (both *X* and *Y* directions) are shown in Fig. 5 (F and G; corresponding positions are marked by the two green arrows in Fig. 5D, respectively). In both cross-sectional scans, a large number of micrometer-sized particles are observed close to the retina near the optic disc. The region away from the optic disc (labeled by the yellow arrow in Fig. 5D) serves as a negative control, where only a negligible number of spots are found near the retina (Fig. 5H). A 3D reconstruction of the OCT scans at the optic disc region (labeled by the white dashed box in Fig. 5D) quantifies the spatial distribution of the micropropellers near the retina. The distribution is displayed as a heat map in Fig. 5E and spots corresponding to the microparticles that are located in the region very close to the optic disc area with a diameter of ~6 mm. Considering that the volume of the injected solution (~100 μl) has a diameter of ~6 mm, the results indicate that the propulsion of the micropropellers shows an excellent directionality under the control of the external magnetic field, which is consistent with the observation of their locomotion under the microscope (Fig. 4, C and D).

The distance from the center of the porcine eye to the retina is ~15 mm. Micropropellers were observed close to the retina by OCT after an actuation period of 30 min, suggesting that the propulsion velocity is at least ~8 μm/s. The velocity is comparable to the velocities measured under the microscope (10 ± 3 μm/s at 70 Hz; Fig. 3F). Therefore, similar active propulsion behavior is achieved in the intact porcine eye, as in a dissected piece of the vitreous. The results indicate that the slippery micropropellers can be manipulated to a target position on the retina and that OCT allows for their noninvasive tracking during ophthalmological applications.

DISCUSSION

We demonstrate that two major criteria should be fulfilled for the propulsion in biological media: (i) matched size of the particles to the macromolecular network and (ii) reduced interaction between the

propellers and the biopolymer network. The slippery micropropellers are designed to have a spherical head with a helical tail, both ~500 nm in diameter to match the mesh size of the vitreous, since a previous study has determined that the particles with a diameter of ~500 nm show a relatively unhindered movement through the biopolymeric network of the porcine vitreous (*6*, *22*). The shape of the helix tail is based on a study that determined the optimal geometry of helical micropropellers (*36*). The microhelical propellers were accomplished by a physical vapor shadow growth technique, which permits the growth of helical magnetic microarchitectures with sizes ranging from the nanoscale to the microscale. Notably, nanosized helical propellers can also move with a high relative velocity of ~3 body lengths per second in biological viscoelastic media (*24*). However, the absolute velocity of 1.5 μm/s is low because of their nanosized body length. Hence, the micropropellers reported herein not only match the mesh size of vitreous network but also achieve a velocity that is almost one order of magnitude faster than the velocity of the nanopropellers.

The strong adhesion between the collagen fibrils and the particles is the other major obstacle for active propulsion of particles through the vitreous (*37*). A number of surface coatings have been compared (table S1), and the perfluorocarbon molecule functionalization with a liquid slippery coating has been found to be most promising for intravitreal propulsion. The coating is plant inspired, drawn from the example of the *Nepenthes* pitcher plant, which uses a perfluorocarbon liquid layer to reduce adhesion. Unlike the antifouling surface of the natural lotus plant that relies on an air-liquid interface (*38*), the perfluorocarbon liquid surface shows exceptional stability under pressure and resists physical damage (*26*), as we observe the propellers' long-time operation (even after months of storage).

The approach reported herein outperforms delivery methods based on passive diffusion in several aspects: First, the targeted region on the retina is as small as ~6 mm in diameter, whereas conventional passive diffusion does not permit the delivery of drugs to a specific region on the retina. Despite large directional fluctuations at short times due to the heterogeneous biopolymer network, the micropropellers maintain excellent long-range directionality when propelled by the magnetic field. Further improvements in the precision of the delivery are possible with a controlled injection system and real-time feedback navigation during the propulsion in the vitreous. Targeted delivery promises lower side effects and a higher efficiency with the proposed technology. Second, the experimental results suggest that the particles can move from the center of the vitreous to the retina in 30 min. The delivery time is ~10 times shorter than that due to passive diffusion of particles of similar size [it has been reported that ~340-nm albumin/hyaluronic acid particles need 6 hours to cover ~1 cm (*39*)].

Most biological tissues are porous: For example, the extracellular matrix has a pore size of approximately 100 to 300 nm (*40*), and the mucus has a pore size of 100 nm to several micrometers (*41*). The propulsion mechanism reported here is general and can be applied to various porous biological media, where the active motion of the propellers holds considerable promise. The biocompatibility and biodegradability of the slippery propeller are important for clinical ocular applications. The materials of the slippery propellers such as silica and perfluorocarbons are classified as a GRAS ("generally regarded as safe") agent and are approved for eye surgery, respectively (*42*, *43*). Although Ni is toxic, it can be replaced with more biocompatible Fe with very similar performance characteristics, as we show herein (figs. S3 and S4).

In summary, we report the first long-range active propulsion of micropropellers through biological tissues. The propulsion is enabled by magnetic helical micropropellers that have a diameter comparable to the mesh size of the medium and a liquid perfluorocarbon coating that effectively minimizes adsorption of the micropropellers to the vitreous. We show that the coated helical micropropellers (0.5 μm in diameter and 2 μm in length) are able to propel in the vitreous body of a porcine eye at a speed of ~10 μm/s. We used a clinical OCT to monitor the movement of the particles and to confirm their arrival at the retina. The long-distance intravitreal propulsion of microrobots in the eye, demonstrated here in combination with clinically noninvasive imaging, lays the basis for targeted delivery in real tissues and potential clinical applications.

MATERIALS AND METHODS

Fabrication of the liquid-coated micropropellers

The uncoated SiO_2-Ni microhelices were prepared using the GLAD method, as previously reported (*32*). A Langmuir-Blodgett (LB) monolayer of 500-nm silica particles was deposited on a 51-mm diameter silicon wafer to be consistent with SI uni silicon wafer (*21*). Nickel (~150 nm) was then deposited onto the silica particles with an angle of incidence of 85° in our customized GLAD system, followed by silica deposited under rotation to form a left-handed helix with 1.8 turns. The wafer containing the microhelices was then treated with an oxygen plasma (PVA TePla 100, Plasma Systems) at 200 mW for 15 s, and the activated wafer containing the micropropellers was then incubated with 20 μl of perfluorocarbon silane (1*H*,1*H*,2*H*,2*H*-perfluorooctyltriethoxysilane) under vacuum for 20 min, followed by heating at 85°C at atmospheric pressure for 1 hour. The microhelices were then immersed in a perfluorocarbon liquid (Fluorinert FC-70, Sigma-Aldrich) and left overnight in a shaker. After rinsing with acetone, the wafer was gently dried under nitrogen. Before the propulsion experiments in the vitreous, the micropropellers were magnetized diametrically by an electromagnet (Walker Scientific Inc.) with a strength of 1.7 T. Micropropellers (on a wafer area of ~6 mm^2) were suspended into 20 μl of phosphate-buffered saline (PBS; pH 7.6) (Thermo Fisher Scientific) by sonication for 3 min before injection into the vitreous.

Characterization techniques

The contact angle was measured with a Dataphysics OCAH 230, and a 3-μl water droplet was deposited on the surfaces (silicon wafer, the silicon wafer with an array of microhelices, the silicon wafer with a slippery perfluorocarbon liquid coating, and the silicon wafer with an array of microhelices coated with the slippery perfluorocarbon coating). The contact angle results are the average of three droplet measurements. The SEM characterization was conducted with a Zeiss Ultra 55 at an operating voltage of 5 keV. A drop of the sample suspension was dropped on a silicon wafer for imaging of the coated micropropellers. FTIR–attenuated total reflection analysis was conducted with a Bruker VERTEX 70v in the single reflection mode at 45°. The magnetization of the microhelix was measured in a superconducting quantum interference device (SQUID). A piece of silicon wafer (~10 mm^2) with deposited microhelices (a total number of ~1.54×10^7) was measured at 300 K by the SQUID magnetometer (Magnetic Property Measurement System, Quantum Design). The magnetization-applied magentic field (M-H) curve of the wafer piece is plotted in fig. S12.

The quantitative dynamic AFM measurements were conducted, as previously reported (*44*, *45*). The morphology and quantitative

nanomechanical measurements with AFM were recorded with a Peakforce Tapping mode using a commercial MultiMode VIII (Bruker) AFM under ambient conditions. Before the measurement, the silicon cantilever (RETSAP-300, Bruker) was calibrated with a standard procedure, and the spring constant, deflection sensitivity, and tip radius were determined to be 38.14 N/m, 26.57 nm/V, and 6 nm, respectively. The quantitative mechanical measurement was performed at a scan frequency of 0.1 Hz, with optimized feedback parameters and a resolution of 512 by 512 pixels. The mechanical properties were all measured using the same cantilevers. All the images and the adhesion distribution were analyzed using the commercial software SPIP (Scanning Probe Image Processor, Image Metrology, Denmark).

Preparation of the vitreous and propulsion experiments under the microscope

Porcine eyes were obtained from a local slaughter house after slaughter, stored on ice for transportation, and kept at 4°C for no more than 36 hours before the experiments. The samples for the microscope propulsion experiments were dissected from the porcine vitreous and used within 30 min after dissection. The sample with a volume of ~10 μl was placed on a glass coverslip (Thermo Fisher Scientific) with a Gene Frame (Thermo Fisher Scientific). Then, ~2 μl of PBS (pH 7.6) buffer solution containing micropropellers was injected into the vitreous using a 10-μl pipette, and the sample was sealed with another piece of coverslip to prevent evaporation. For the control experiment, ~2 μl of PBS buffer solution containing micropropellers was injected into the 25% glycerol with the same process as the vitreous treatment. The sample was placed at the center of three orthogonal pairs of custom Helmholtz coils and observed under a microscope (Zeiss Observer) [objective, 50× and numerical aperture (NA) = 0.5 or objective, 100× and NA = 0.75]. The movies were captured using a complementary metal-oxide semiconductor camera (Andor Zyla) at ~48 frames per second, with 60N-C 1″ 1.0× Adapter (Zeiss) for the 50× objective and a 1.6× C-Mount Adapter (Best Scientific) for the 100× objective, respectively. ImageJ (version 1.51p, National Institutes of Health) was used to track the movement of the slippery micropropellers with the plugin Manual Tracking. The driving magnetic field has a strength of 8 mT, and the rotational frequency was swept from 10 to 80 Hz in a step of 10 Hz for the propulsion in the vitreous and 25% glycerol, and it was swept from 10 to 140 Hz in a step of 10 Hz for the propulsion in water. Five movies were taken for each frequency, and at least 20 propellers were tracked to calculate the average velocity and the SDs.

Stability of the slippery coating under physiological conditions

To investigate the slippery coating over a longer period, the micropropellers were placed in physiological PBS buffers, and the wafer containing the slippery helices was incubated with 5% (w/v) bovine serum albumin under stirring at 500 rpm for a period ranging from 0 to 2 hours. The propulsion performance was evaluated after the exposure by determining the percentage of propellers that showed successful propulsion in vitreous.

Fluorescence imaging of the micropropellers

To prepare the fluorescent nanodiamond–functionalized slippery micropropellers, the oxygen plasma–treated microhelices were immersed into the toluene solution containing 1% (v/v) 3-aminopropyltriethoxysilane (Sigma-Aldrich) and 0.01% (v/v) triethanolamine at 75°C overnight (*46*). After washing with toluene, acetone, and water, the wafer was then incubated with nanodiamonds [0.1 mg/ml; 40 nm in diameter, carboxylic groups; Adámas Nanotechnologies], 200 mM 1-ethyl-3-(3-dimethylaminopropyl)carbodiimide, and 50 mM *N*-hydroxysuccinimide in 0.1 M acetic acid at pH 5 overnight under intensive stirring (*47*). To functionalize the slippery layer onto the microhelices, an Al_2O_3 adhesion layer with a thickness of 10 nm was deposited onto the microhelix wafer via atomic layer deposition (ALD) for 100 cycles by repeatedly pulsing the trimethylaluminum precursors and water for 0.15 s, respectively. The ALD and nanodiamond-functionalized wafer with microhelix patterns was subjected to the same coating procedure as the uncoated microhelix wafer.

A ~3-mm incision was made, and 100 μl of solution containing the fluorescent slippery micropropellers was injected into the center of the vitreous using a 100-μl pipette. The eye was placed in a magnetic field of 80 mT rotating at 70 Hz. After the magnetic propulsion, the porcine eye was cut with a scalpel, followed by mechanically removing the vitreous, cutting the sclera into squares (1 cm by 1 cm) according to the report (*48*), and staining with DAPI. The fluorescence of the propellers was excited by a light-emitting diode (LED) (Illumination system Colibri.2, Carl Zeiss Microscopy) with a center wavelength of 470 nm, and the fluorescent images were captured through a beam splitter HC BS 409 (AHF Analysentechnik AG) and a filter (607/36 BrightLine HC, AHF Analysentechnik AG). The fluorescence of DAPI was excited by a LED with a center wavelength of 365 nm, and the images were captured through a beam splitter HC-Quadband (AHF Analysentechnik AG) and a filter (409/LP Longpass Filter BrightLine, AHF Analysentechnik AG). The experiment was independently repeated three times.

OCT imaging of the micropropellers

The microhelices were mixed with 20-μm silica microparticles (~0.02%; sicastar-greenF, micromod Partikeltechnologie GmbH). A ~3-mm incision was made, and 100 μl of solution was injected into the center of the vitreous using a 100-μl pipette. The eye was then placed at the center of a custom-built three-axis Helmholtz coil setup. A rotational magnetic field with a strength of 8 mT and a frequency of 70 Hz was applied. The rotational axis was pointed toward the optic disc region of the retina, and the rotational direction was counterclockwise (viewing from the side of the lens). The eye was then placed on the imaging instrument that combines scanning laser imaging and high-resolution OCT [SPECTRALIS Heidelberg Engineering Retinal Angiography (HRA)+OCT, Heidelberg Engineering GmbH] by a custom holder. Fluorescent silica particles were imaged under a 485-nm laser excitation and a 510-nm emission filter in the HRA mode. The slippery micropropellers were imaged by OCT scans with both 19 slices in *X* and *Y* directions, respectively. The experiment was independently repeated three times. Counting of micropropellers in each OCT scan was conducted, and pseudocolor images were generated by a custom script in MATLAB (R2017a, MathWorks).

SUPPLEMENTARY MATERIALS

Supplementary material for this article is available at http://advances.sciencemag.org/cgi/content/full/4/11/eaat4388/DC1

Fig. S1. Schematic of the experimental scheme used to confirm the movement of the propellers in the vitreous.

Fig. S2. Intravitreal propulsion of micropropellers with different coatings.

Fig. S3. SEM images of the micropropellers grown with TiO_2 and Fe.

Fig. S4. Time-lapse images showing the controlled movement (forward/backward) of the slippery Fe-containing propellers when actuated by the external magnetic field.
Fig. S5. Percentage of propelling micropropellers containing Ni (black) and those made with Fe (red) in vitreous with different surface coatings.
Fig. S6. Percentage of propelling slippery propellers in vitreous before and after incubation within 5% bovine serum albumin in PBS solution for 2 hours.
Fig. S7. Characterization of the surface coating on the micropropellers by AFM.
Fig. S8. Intravitreal propulsion of the slippery propellers as a function of the magnetic field strength.
Fig. S9. Propulsion of the slippery micropropellers in glycerol solution.
Fig. S10. Fluorescence images of the excised retina.
Fig. S11. Investigation of the distribution of the propellers on the retina.
Fig. S12. The M-H curve of a wafer piece (area of 10 mm^2) containing an array of microhelices.
Table S1. Statistical analysis of micropropellers moving in vitreous as a function of the surface coating.
Movie S1. Wobbling motion of an uncoated micropropeller in the vitreous under the actuation of a rotating magnetic field with a strength of 8 mT and a frequency of 6 Hz.
Movie S2. Propulsion of a slippery micropropeller in the vitreous under the actuation of a rotating magnetic field with a strength of 8 mT and a frequency of 6 Hz.
Movie S3. A large swarm of slippery micropropellers moves across the boundary of an aqueous buffer into the vitreous and continues propelling in the vitreous under a rotating magnetic field with a strength of 8 mT and a frequency of 70 Hz.
Movie S4. Controlled motion of slippery micropropellers in the vitreous under a rotating magnetic field with a strength of 8 mT and a frequency of 50 Hz.
Movie S5. OCT shows the distribution of the slippery micropropellers at the vitreous-retina boundary.

REFERENCES AND NOTES

1. A. Patel, K. Cholkar, V. Agrahari, A. K. Mitra, Ocular drug delivery systems: An overview. *World J. Pharmacol.* **2**, 47–64 (2013).
2. S. Resnikoff, D. Pascolini, D. Etya'ale, I. Kocur, R. Pararajasegaram, G. P. Pokharel, S. P. Mariotti, Global data on visual impairment in the year 2002. *Bull. World Health Organ.* **82**, 844–851 (2004).
3. P. M. Hughes, O. Olejnik, J.-E. Chang-Lin, C. G. Wilson, Topical and systemic drug delivery to the posterior segments. *Adv. Drug Deliv. Rev.* **57**, 2010–2032 (2005).
4. A. Urtti, Challenges and obstacles of ocular pharmacokinetics and drug delivery. *Adv. Drug Deliv. Rev.* **58**, 1131–1135 (2006).
5. H.-Y. Zhou, J.-L. Hao, S. Wang, Y. Zheng, W.-S. Zhang, Nanoparticles in the ocular drug delivery. *Int. J. Ophthamol.* **6**, 390–396 (2013).
6. Q. Xu, N. J. Boylan, J. S. Suk, Y.-Y. Wang, E. A. Nance, J.-C. Yang, P. J. McDonnell, R. A. Cone, E. J. Duh, J. Hanes, Nanoparticle diffusion in, and microrheology of, the bovine vitreous ex vivo. *J. Control. Release* **167**, 76–84 (2013).
7. B. T. Käsdorf, F. Arends, O. Lieleg, Diffusion regulation in the vitreous humor. *Biophys. J.* **109**, 2171–2181 (2015).
8. A. J. Witkin, G. C. Brown, Update on nonsurgical therapy for diabetic macular edema. *Curr. Opin. Ophthalmol.* **22**, 185–189 (2011).
9. K. G. Janoria, S. Gunda, S. H. Boddu, A. K. Mitra, Novel approaches to retinal drug delivery. *Expert Opin. Drug Deliv.* **4**, 371–388 (2007).
10. J. Wang, *Nanomachines: Fundamentals and Applications* (Wiley-VCH, 2013).
11. W. Qin, T. Peng, Y. Gao, F. Wang, X. Hu, K. Wang, J. Shi, D. Li, J. Ren, C. Fan, Catalysis-driven self-thermophoresis of Janus plasmonic nanomotors. *Angew. Chem. Int. Ed.* **56**, 515–518 (2017).
12. D. Fan, Z. Yin, R. Cheong, F. Q. Zhu, R. C. Cammarata, C. L. Chien, A. Levchenko, Subcellular-resolution delivery of a cytokine through precisely manipulated nanowires. *Nat. Nanotechnol.* **5**, 545–551 (2010).
13. B. Dai, J. Wang, Z. Xiong, X. Zhan, W. Dai, C.-C. Li, S.-P. Feng, J. Tang, Programmable artificial phototactic microswimmer. *Nat. Nanotechnol.* **11**, 1087–1092 (2016).
14. B. E.-F. de Ávila, P. Angsantikul, J. Li, M. A. Lopez-Ramirez, D. E. Ramírez-Herrera, S. Thamphiwatana, C. Chen, J. Delezuk, R. Samakapiruk, V. Ramez, M. Obonyo, L. Zhang, J. Wang, Micromotor-enabled active drug delivery for in vivo treatment of stomach infection. *Nat. Commun.* **8**, 272 (2017).
15. W. Gao, R. Dong, S. Thamphiwatana, J. Li, W. Gao, L. Zhang, J. Wang, Artificial micromotors in the mouse's stomach: A step toward in vivo use of synthetic motors. *ACS Nano* **9**, 117–123 (2015).
16. J. Li, B. E.-F. de Ávila, W. Gao, L. Zhang, J. Wang, Micro/nanorobots for biomedicine: Delivery, surgery, sensing, and detoxification. *Sci. Robot.* **2**, eaam6431 (2017).
17. P. L. Venugopalan, R. Sai, Y. Chandorkar, B. Basu, S. Shivashankar, A. Ghosh, Conformal cytocompatible ferrite coatings facilitate the realization of a nanovoyager in human blood. *Nano Lett.* **14**, 1968–1975 (2014).
18. R. Cheng, W. Huang, L. Huang, B. Yang, L. Mao, K. Jin, Q. ZhuGe, Y. Zhao, Acceleration of tissue plasminogen activator-mediated thrombolysis by magnetically powered nanomotors. *ACS Nano* **8**, 7746–7754 (2014).
19. A. Ghosh, P. Fischer, Controlled propulsion of artificial magnetic nanostructured propellers. *Nano Lett.* **9**, 2243–2245 (2009).
20. A. Servant, F. Qiu, M. Mazza, K. Kostarelos, B. J. Nelson, Controlled in vivo swimming of a swarm of bacteria-like microrobotic flagella. *Adv. Mater.* **27**, 2981–2988 (2015).
21. D. Walker, B. T. Käsdorf, H.-H. Jeong, O. Lieleg, P. Fischer, Enzymatically active biomimetic micropropellers for the penetration of mucin gels. *Sci. Adv.* **1**, e1500501 (2015).
22. F. Ullrich, C. Bergeles, J. Pokki, O. Ergeneman, S. Erni, G. Chatzipirpiridis, S. Pané, C. Framme, B. J. Nelson, Mobility experiments with microrobots for minimally invasive intraocular surgery. *Invest. Ophthalmol. Vis. Sci.* **54**, 2853–2863 (2013).
23. T. Qiu, D. Schamel, A. G. Mark, P. Fischer, Active microrheology of the vitreous of the eye applied to nanorobot propulsion, in *2014 IEEE International Conference on Robotics and Automation (ICRA)* (IEEE, 2014), pp. 3801–3806.
24. D. Schamel, A. G. Mark, J. G. Gibbs, C. Miksch, K. I. Morozov, A. M. Leshansky, P. Fischer, Nanopropellers and their actuation in complex viscoelastic media. *ACS Nano* **8**, 8794–8801 (2014).
25. H. F. Bohn, W. Federle, Insect aquaplaning: Nepenthes pitcher plants capture prey with the peristome, a fully wettable water-lubricated anisotropic surface. *Proc. Natl. Acad. Sci. U.S.A.* **101**, 14138–14143 (2004).
26. T.-S. Wong, S. H. Kang, S. K. Y. Tang, E. J. Smythe, B. D. Hatton, A. Grinthal, J. Aizenberg, Bioinspired self-repairing slippery surfaces with pressure-stable omniphobicity. *Nature* **477**, 443–447 (2011).
27. D. C. Leslie, A. Waterhouse, J. B. Berthet, T. M. Valentin, A. L. Watters, A. Jain, P. Kim, B. D. Hatton, A. Nedder, K. Donovan, E. H. Super, C. Howell, C. P. Johnson, T. L. Vu, D. E. Bolgen, S. Rifai, A. R. Hansen, M. Aizenberg, M. Super, J. Aizenberg, D. E. Ingber, A bioinspired omniphobic surface coating on medical devices prevents thrombosis and biofouling. *Nat. Biotechnol.* **32**, 1134–1140 (2014).
28. J. Chen, C. Howell, C. A. Haller, M. S. Patel, P. Ayala, K. A. Moravec, E. Dai, L. Liu, I. Sotiri, M. Aizenberg, An immobilized liquid interface prevents device associated bacterial infection in vivo. *Biomaterials* **113**, 80–92 (2017).
29. Y. K. Chan, N. Cheung, W. S. Chan, D. Wong, Quantifying silicone oil emulsification in patients: Are we only seeing the tip of the iceberg? *Graefes Arch. Clin. Exp. Ophthalmol.* **253**, 1671–1675 (2015).
30. M. M. Hawkeye, M. J. Brett, Glancing angle deposition: Fabrication, properties, and applications of micro- and nanostructured thin films. *J. Vac. Sci. Technol. A* **25**, 1317–1335 (2007).
31. K. Robbie, J. C. Sit, M. J. Brett, Advanced techniques for glancing angle deposition. *J. Vac. Sci. Technol. B Microelectron. Nanometer Struct. Process Meas. Phenom.* **16**, 1115–1122 (1998).
32. A. G. Mark, J. G. Gibbs, T.-C. Lee, P. Fischer, Hybrid nanocolloids with programmed three-dimensional shape and material composition. *Nat. Mater.* **12**, 802–807 (2013).
33. H. Zhou, H. Wang, H. Niu, A. Gestos, X. Wang, T. Lin, Fluoroalkyl silane modified silicone rubber/nanoparticle composite: A super durable, robust superhydrophobic fabric coating. *Adv. Mater.* **24**, 2409–2412 (2012).
34. B. Lee, M. Litt, G. Buchsbaum, Rheology of the vitreous body: Part 2. Viscoelasticity of bovine and porcine vitreous. *Biorheology* **31**, 327–338 (1994).
35. M. Medina-Sánchez, O. G. Schmidt, Medical microbots need better imaging and control. *Nature* **545**, 406–408 (2017).
36. D. Walker, M. Kübler, K. I. Morozov, P. Fischer, A. M. Leshansicy, Optimal length of low Reynolds number nanopropellers. *Nano Lett.* **15**, 4412–4416 (2015).
37. L. Peeters, N. N. Sanders, K. Braeckmans, K. Boussery, J. Van de Voorde, S. C. De Smedt, J. Demeester, Vitreous: A barrier to nonviral ocular gene therapy. *Invest. Ophthalmol. Vis. Sci.* **46**, 3553–3561 (2005).
38. L. Jiang, Y. Zhao, J. Zhai, A lotus-leaf-like superhydrophobic surface: A porous microsphere/nanofiber composite film prepared by electrohydrodynamics. *Angew. Chem. Int. Ed. Engl.* **43**, 4338–4341 (2004).
39. H. Koo, H. Moon, H. Han, J. H. Na, M. S. Huh, J. H. Park, S. J. Woo, K. H. Park, I. C. Kwon, K. Kim, H. Kim, The movement of self-assembled amphiphilic polymeric nanoparticles in the vitreous and retina after intravitreal injection. *Biomaterials* **33**, 3485–3493 (2012).
40. R. M. Kuntz, W. M. Saltzman, Neutrophil motility in extracellular matrix gels: Mesh size and adhesion affect speed of migration. *Biophys. J.* **72**, 1472–1480 (1997).
41. S. K. Lai, Y.-Y. Wang, J. Hanes, Mucus-penetrating nanoparticles for drug and gene delivery to mucosal tissues. *Adv. Drug Deliv. Rev.* **61**, 158–171 (2009).
42. J. G. Croissant, Y. Fatieiev, N. M. Khashab, Degradability and clearance of silicon, organosilica, silsesquioxane, silica mixed oxide, and mesoporous silica nanoparticles. *Adv. Mater.* **29**, 1604634 (2017).
43. M. Soheilian, G. A. Peyman, H. Wafapoor, G. C. Navarro, H. Thompson, Surgical management of traumatic retinal detachment with perfluorocarbon liquid. *Int. Ophthalmol.* **20**, 241–249 (1996).
44. D. Xia, S. Zhang, J. Ø. Hjortdal, Q. Li, K. Thomsen, J. Chevallier, F. Besenbacher, M. Dong, Hydrated human corneal stroma revealed by quantitative dynamic atomic force microscopy at nanoscale. *ACS Nano* **8**, 6873–6882 (2014).

45. L. Liu, Q. Li, S. Zhang, X. Wang, S. V. Hoffman, J. Li, Z. Liu, F. Besenbacher, M. Dong, Identification of a novel parallel β-strand conformation within molecular monolayer of amyloid peptide. *Adv. Sci.* **3**, 1500369 (2016).
46. J. A. Howarter, J. P. Youngblood, Optimization of silica silanization by 3-aminopropyltriethoxysilane. *Langmuir* **22**, 11142–11147 (2006).
47. J. Benesch, P. Tengvall, Blood protein adsorption onto chitosan. *Biomaterials* **23**, 2561–2568 (2002).
48. K. Januschowski, S. Müller, C. Krupp, M. S. Spitzer, J. Hurst, M. Schultheiss, K.-U. Bartz-Schmidt, P. Szurman, S. Schnichels, Glutamate and hypoxia as a stress model for the isolated perfused vertebrate retina. *J. Vis. Exp.* **2015**, 52270 (2015).

Acknowledgments: We are grateful to C. Miksch for LB deposition and GLAD, J. P. Spatz for SEM access, S. Jagiella for the help with FTIR, G. Schütz for SQUID access, and J. Hurst for the histological section. We thank Q. He, B. E.-F. de Ávila, F. Serwane, and U. Choudhury for helpful discussions. **Funding:** The research was in part supported by the European Research Council under the ERC Grant Agreement Chiral MicroBots (no. 278213) and by the Max Planck Society. Z. Wu was supported by the Alexander von Humboldt Foundation. M.D. would like to thank the EU H2020RISE, 2016-MNR4S Cell project. **Author contributions:** P.F., Z. Wu, and T.Q. conceived the project. P.F. and T.Q. supervised the studies. Z. Wu, H.-H.J., Q.W., and T.Q. carried out the preparation and the characterization of the micropropellers. Z. Wu, T.Q., and J.T. characterized the movement of the micropropellers. M.S., F.Z., and S.S. conducted the OCT and SLO experiments. Z. Wang and M.D. conducted AFM experiments. Z. Wu, T.Q., and P.F. interpreted the data and co-wrote the paper. **Competing interests:** Z. Wu, T.Q., and P.F. are inventors on a patent application related to this work filed by Max Planck Innovation GmbH (EP17187924.0, filed 25 August 2017). P.F. is an inventor on a patent related to this work filed by Max Planck Innovation GmbH (US8768501B2, granted 1 April 2014). All other authors declare that they have no competing interests. **Data and materials availability:** All data needed to evaluate the conclusions in the paper are present in the paper and/or the Supplementary Materials. Additional data related to this paper may be requested from the authors.

Submitted 26 February 2018
Accepted 25 September 2018
Published 2 November 2018
10.1126/sciadv.aat4388

Citation: Z. Wu, J. Troll, H.-H. Jeong, Q. Wei, M. Stang, F. Ziemssen, Z. Wang, M. Dong, S. Schnichels, T. Qiu, P. Fischer, A swarm of slippery micropropellers penetrates the vitreous body of the eye. *Sci. Adv.* **4**, eaat4388 (2018).